

沉积路径对激光诱导 MIG 增材 2319 铝合金的影响

靳佩昕, 张兆栋*, 马紫成, 宋刚, 刘黎明

大连理工大学材料科学与工程学院辽宁省先进连接技术重点实验室, 辽宁 大连 116024

摘要 采用基于激光诱导熔化极惰性气体保护(melt inert gas, MIG)电弧焊的增材技术,研究了插补沉积和交叉沉积两种不同沉积路径对 2319 铝合金块体组织性能的影响。结果表明:插补沉积的晶粒细小,柱状晶生长方向一致;交叉沉积的晶粒粗大,柱状晶生长方向杂乱无章。在力学性能上,插补沉积和交叉沉积的平均硬度分别是 97.9 HV 和 89.2 HV,交叉沉积下试件的整体硬度分布更均匀。插补沉积试件的强度和塑性具有各向异性,交叉沉积试件的强度和塑性具有各向同性。其中,插补沉积试件沿 X 方向和 Y 方向的抗拉强度分别为 233.58 MPa 和 275.52 MPa,延伸率分别为 6.34% 和 11.12%。交叉沉积试件在 XY 平面的极限抗拉强度为 251.33 MPa,延伸率为 7.68%。研究表明,对于铝合金块体的激光诱导 MIG 增材技术制造,插补沉积试件在 Y 方向上的整体组织性能优于交叉沉积试件。

关键词 激光技术; 激光诱导电弧; 路径; 增材制造; 2319 铝合金; 组织性能; 扫描电镜

中图分类号 TG444+.2

文献标志码 A

DOI: 10.3788/CJL202249.1402205

1 引言

近年来,与传统的减材制造相比,增材制造(additive manufacturing, AM)因在结构轻巧性、零件外形自由性、材料高利用性以及功能梯度材料的可制造性上具有巨大优势而发展迅速^[1]。据统计,2013—2019 年我国增材制造领域一直维持着 40% 的增长速度,产业规模逐渐扩大^[2]。增材制造有三类热源,其中电弧熔丝增材制造(wire arc additive manufacturing, WAAM)技术就具有高堆积速率、高利用率、低费用及适用于制造大型构件的优势,是一种具有发展潜力的增材制造方法^[3]。

在全球节能减排的背景下,铝合金是一种高性能轻型合金,使用增材技术可以实现整体化、复杂化铝合金零件的制造^[4]。同时,WAAM 的低成本高效率等优势吸引了大批学者对其进行研究。研究者基于冷金属过渡(cold metal transfer, CMT)电弧增材工艺对铝合金 WAAM 技术进行了系统性研究,分析了焊丝质量、熔滴过渡模式、保护气流量、层间碾压压力等因素对铝合金 WAAM 结构气孔及力学性能的影响^[5-7]。国内学者 Ren 等^[8]采用 CMT 技术对 Al-6.3Mg 进行了单道多层薄壁件的增材制造,以层间温度为变量进行了四组试验,结果表明,降低层间温度能有效提高沉积层性能,减小各向异性。Wu 等^[9]在传统的 WAAM 系统基础上加了热丝装置,从而提高了沉积效率,降低

了气孔率。李旭文等^[10]发现,激光诱导钨极氩弧(tungsten inert gas, TIG)复合技术可以提高不锈钢增材制造过程的稳定性,压缩电弧,提高堆积速度和效率,实现低热输入的增材制造。

目前,关于铝合金增材制造的多数研究重点仍集中在单道多层薄壁件,关于多层多道电弧增材制造的研究较少。路径策略是 WAAM 的第一步,多道电弧增材制造时不同堆积路径的散热条件存在差异,导致试件组织性能不同,因此选择合适的路径有利于提高零件的性能^[11]。刘黎明等^[12]采用平行往复、十字正交和插补堆积三种路径电弧增材制造了 316 不锈钢块体,发现路径对试件组织性能的影响较大。Thijs 等^[13]发现,每层相邻道的扫描方向对激光增材铝合金成形样件的温度梯度及生长速度有显著影响。Prashanth 等^[14]通过调整扫描方式,制备了有轮廓和无轮廓两种铝合金块体试样,发现不同路径对微观组织和缺陷有影响,直接决定了成形件的力学性能。由于单电弧增材铝合金气孔较多、性能较差,孙承帅等^[15]使用基于低功率激光-熔化极惰性气体保护(melt inert gas, MIG)电弧焊的复合增材技术制备了铝合金薄壁件,发现加入激光能细化组织,减少气孔含量。综上所述,本文研究了不同堆积路径下 2319 铝合金的低功率激光诱导 MIG 增材制造,探究了不同路径对沉积件组织性能的影响。

收稿日期: 2021-12-22; 修回日期: 2021-12-24; 录用日期: 2022-03-03

基金项目: 国家自然科学基金(U1960111)

通信作者: *skyezzd@dlut.edu.cn

2 试验材料及方法

2.1 材料与设备

试验采用直径为 1.2 mm 的 ER2319 铝合金丝, 化学成分如表 1 所示, 基板采用 2219 铝合金板。该增材制造系统包括一台 OTC FD-V20 机器人、一台 WB-P500L 焊机和一台 LWS-800FK 脉冲激光器。本文所采用的热源是由电弧和低功率脉冲激光组成的复合热源。MIG 焊枪与基底间的夹角为 70° , 激光和焊枪的夹角是 45° 。复合焊枪原理图如图 1 所示。沉积

表 1 ER2319 焊丝的化学成分

Table 1 Chemical compositions of ER2319 welding wire

Composition	Cu	Si	Mn	Fe	Zr	V	Ti	Zn	Al
Mass fraction / %	5.80-6.80	0.04	0.20-0.40	0.30	0.10-0.25	0.07	0.10-0.20	≤ 0.10	Bal.

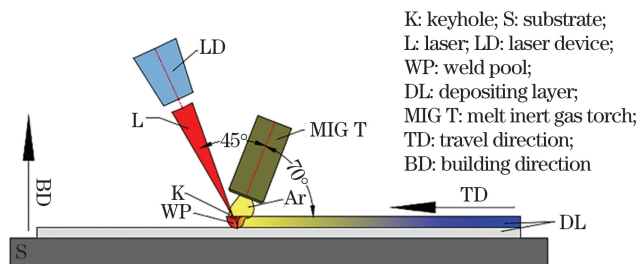


图 1 低功率激光诱导 MIG 电弧增材制造过程示意图
Fig. 1 Schematic of low power laser induced MIG arc additive process

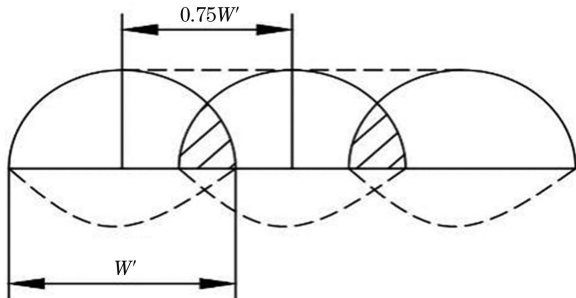


图 2 单层条纹覆盖沉积方式

Fig. 2 Single layer stripe covering deposition mode

2.2 试验方法

本试验采用两种沉积路径, 一种是插补沉积方法, 如图 3(a) 所示, 沿 Y 轴方向沉积, 相邻层焊接方向相反, 共沉积 4 层, 每层 8 道, 其中第一层以后每个焊道在前一层两条焊道之间。另一种是十字交叉沉积方法, 如图 3(b) 所示, 奇数层焊接方向沿 Y 轴正向, 偶数层沉积方向沿 X 轴正向, 沉积 5 层, 每层 8 道。采用光学显微镜观察试件的微观组织。使用扫描电镜 (SEM) 对沉积试样进行微观形貌观察并进行能谱分析。在横截面上选取靠近试件基板的 $8\text{ mm} \times 10\text{ mm}$ 中心区域, 每隔 0.5 mm 测量一次维氏硬度, 从而获取试件面的硬度云图, 测试时载荷为 2 N , 保荷时间为 10 s 。分别沿 X 轴和 Y 轴对试件进行取样, 采用万能拉伸机测试试件的拉伸性能, 取样方法如图 4 所示, 并

前用钢丝刷、丙酮等去除表面杂质及氧化层。本试验用的保护气体是氩气, 纯度 (质量分数) 为 99.99% , 流速为 20 L/min 。焊接电流为 140 A , 平均激光功率为 300 W , 扫描速度为 450 mm/min , 送丝速度与焊接电流自动匹配。如图 2 所示, 单层沉积道间的搭接率为 25% , 使沉积层表面趋于平面, 底部虚线区域是两层间的重熔部分, 其中 W' 代表沉积条纹宽度。焊丝干伸长为 11 mm 。每道堆积完以后的道间冷却时间为 30 s , 每层堆积完以后的层间冷却时间为 60 s 。

对拉伸断口进行观察。

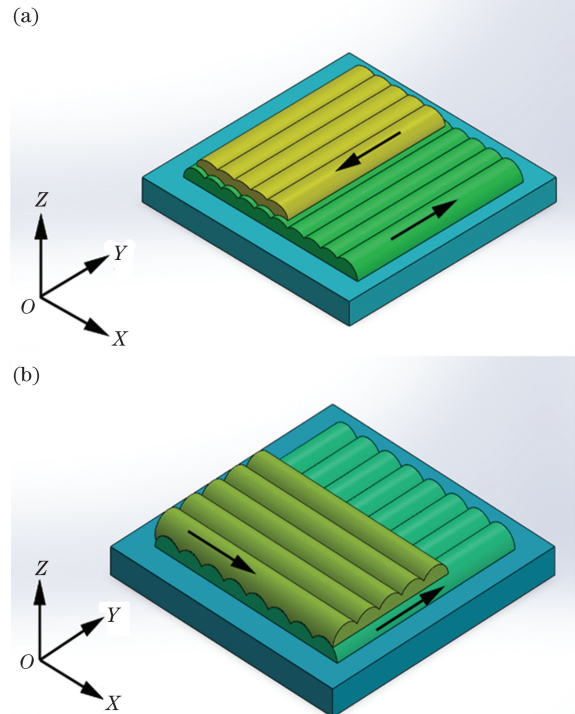


图 3 两种不同沉积路径图。(a) 插补沉积; (b) 十字交叉沉积
Fig. 3 Schematics of two different deposition paths.
(a) Unidirectional linear deposition; (b) crisscross deposition

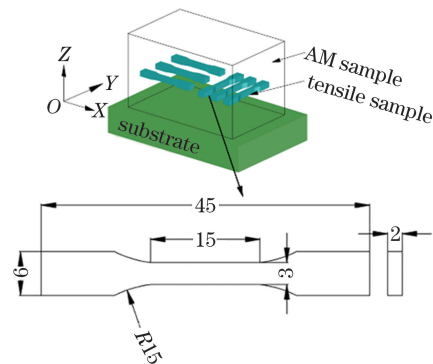


图 4 拉伸取样示意图

Fig. 4 Schematic of tensile sampling

3 分析与讨论

3.1 不同路径增材下的宏观形貌对比

图 5 是两种路径下的宏观截面熔合形貌,其中 W 和 H 分别为单个沉积条纹的宽和高。图 5(a) 为插补沉积,其横截面表现出均匀的鱼鳞状,层与层之

间的波浪线明显。其单个沉积条纹的平均宽度为 7.5 mm,平均高度为 2.3 mm。图 5(b) 为十字交叉沉积,其横截面上的鱼鳞状和条状交替出现。鱼鳞状单个沉积条纹的平均宽度为 7.5 mm,平均高度为 2.1 mm。条状单个沉积条纹的平均宽度为 7.3 mm,平均高度为 2.5 mm。

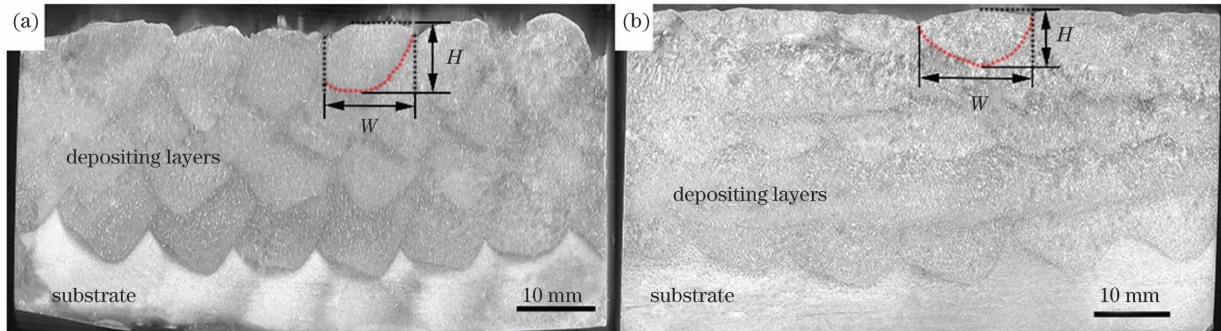


图 5 不同沉积路径下的宏观截面熔合形貌图。(a)插补沉积;(b)十字交叉沉积

Fig. 5 Macroscopic cross-sectional fusion morphologies under different deposition paths. (a) Unidirectional linear deposition; (b) crisscross deposition

分析认为,插补沉积方法中相邻层的焊接方向是相反的,但在同一个轴向上,宏观截面由所有沉积纹的横截面组成。在十字交叉沉积方法中,由于焊接方向发生 90° 变化,宏观截面沉积纹的横截面和侧面交替出现。插补沉积方法中每层条纹沿着同一个方向排列堆积,而十字交叉沉积方法中相邻层的条纹是相互垂直的。

3.2 不同路径增材下的微观组织分布

图 6 是插补沉积下不同位置的微观组织图,插补沉积的底部[图 6(a)]组织是树枝晶,中部[图 6(b)]组织是具有方向性的柱状晶,顶部[图 6(c)]组织由细小的树枝晶组成。图 7 是十字交叉沉积下不同位置的

微观组织图,十字交叉沉积的底部[图 7(a)]组织是树枝晶,中部[图 7(b)]组织是杂乱无章的柱状晶,顶部[图 7(c)]组织是树枝晶。图 8 为过渡区域的微观组织,X 轴正向是铝合金的沉积方向。插补沉积下母材与沉积层过渡区[图 8(a)]是一层细小的等轴晶。在层与层的过渡区[图 8(b)]可以看到明显的过渡线,过渡区组织是粗大的等轴晶。十字交叉沉积下母材与沉积层过渡区[图 8(c)]是一层细小等轴晶。在层与层之间的过渡区[图 8(d)]看不到明显的过渡线,可以观察到大量粗大的等轴晶。气孔缺陷主要出现在层与层之间的过渡区域,十字交叉沉积下的气孔较多。

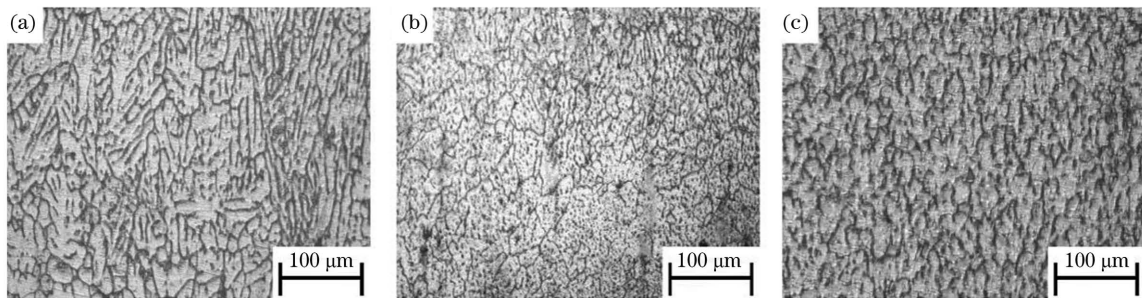


图 6 插补沉积下不同位置的微观组织图。(a)底部;(b)中部;(c)顶部

Fig. 6 Microstructures at different positions under unidirectional linear deposition. (a) Bottom; (b) middle; (c) top

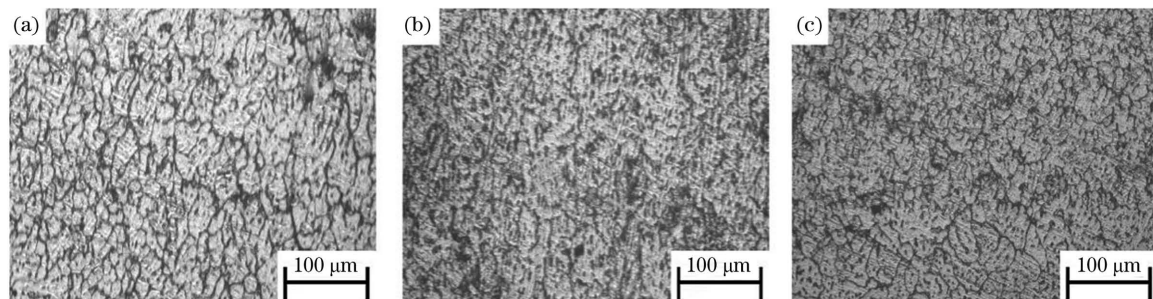


图 7 十字交叉沉积下不同位置的微观组织图。(a)底部;(b)中部;(c)顶部

Fig. 7 Microstructures at different positions under crisscross deposition. (a) Bottom; (b) middle; (c) top

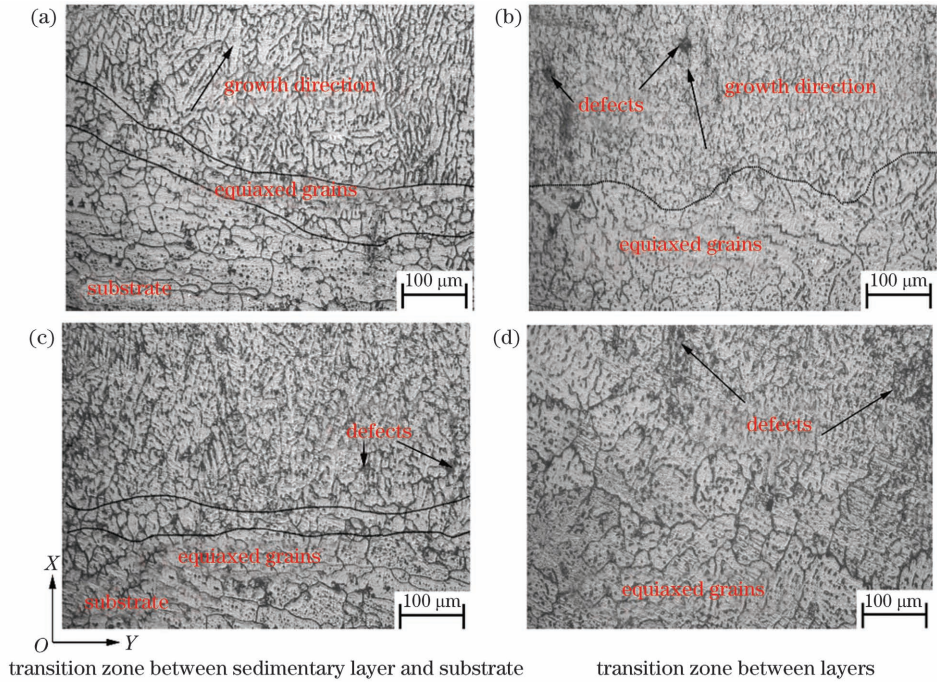


图 8 不同沉积路径下过渡层的微观组织。(a)(b)插补沉积;(c)(d)十字交叉沉积

Fig. 8 Microstructures of transition zone under different deposition paths. (a)(b) Unidirectional linear deposition; (c)(d) crisscross deposition

分析认为,不同路径下的增材制造在熔池底部的冷却速度快,形成了等轴晶,插补沉积下内部胞状晶向熔池中心生长,形成柱状晶^[16],且生长方向一致,表现为各向异性。十字交叉沉积下每层的沉积方向会发生90°变化,不同位置的受热不同,柱状晶的生长方向紊乱,表现为各向同性。顶部由树枝晶组成并且多次枝晶发达,由于试件顶层的表面散热趋势与垂直方向的散热趋势达到了平衡,结晶状态转变为树枝晶。

母材与沉积层过渡区出现细小等轴晶,熔池底部的冷却速度快,形成了等轴晶,且激光对熔池的搅拌作用也可以细化晶粒^[17]。层与层之间的过渡区出现了粗大的等轴晶,这是由于在沉积过程中,熔池在先前堆

积好的沉积层表面不断推进和转移,热量不断向相邻的沉积层传递,这种热处理效果造成了相对较低的冷却速率。而且,在金属凝固时气体来不及析出,产生缺陷。由于十字交叉沉积下不同层的焊接方向不同,晶粒生长没有明显的方向性,故过渡不明显,过渡区大,缺陷更多。

图 9 是沉积层的能谱仪 (energy disperse spectroscopy, EDS) 分析结果,点 2 处 Al 与 Cu 的质量比为 97.18/2.82,可以得出灰色基体是 α(Al) 固溶体,在晶界处,点 1 处 Al 与 Cu 的质量比为 69.63/30.17,其比例接近 Al-Cu 合金的共晶组织的质量比为 67/33^[18]。图 10 是高倍镜组织图,右上角为

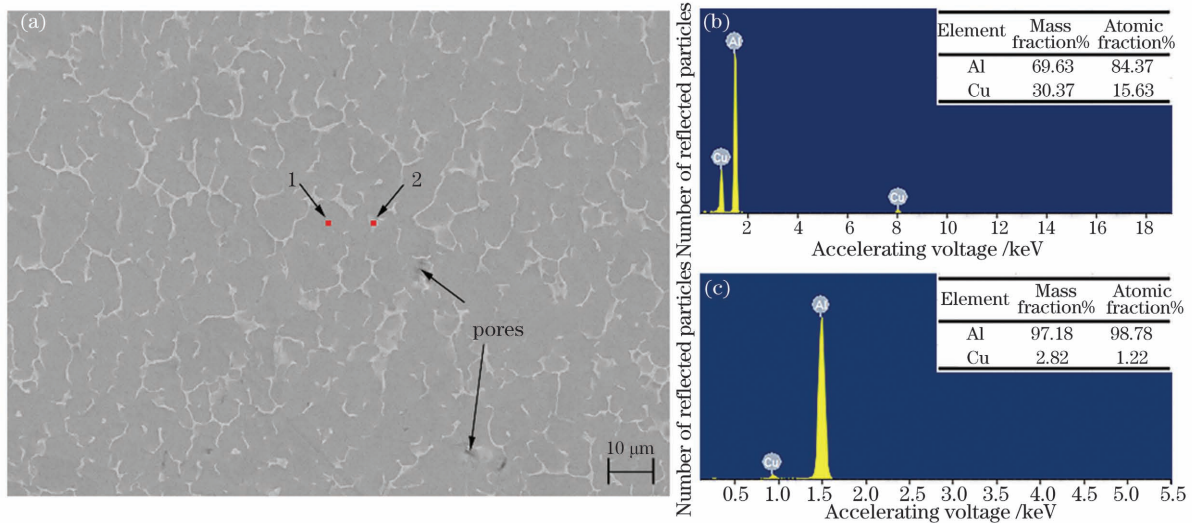


图 9 沉积层 EDS 结果。(a)高倍镜下的显微组织;(b)点 1 处的 EDS 结果;(c)点 2 处的 EDS 结果

Fig. 9 EDS results of sedimentary layer. (a) Microstructure under high magnification; (b) EDS result at point 1; (c) EDS result at point 2

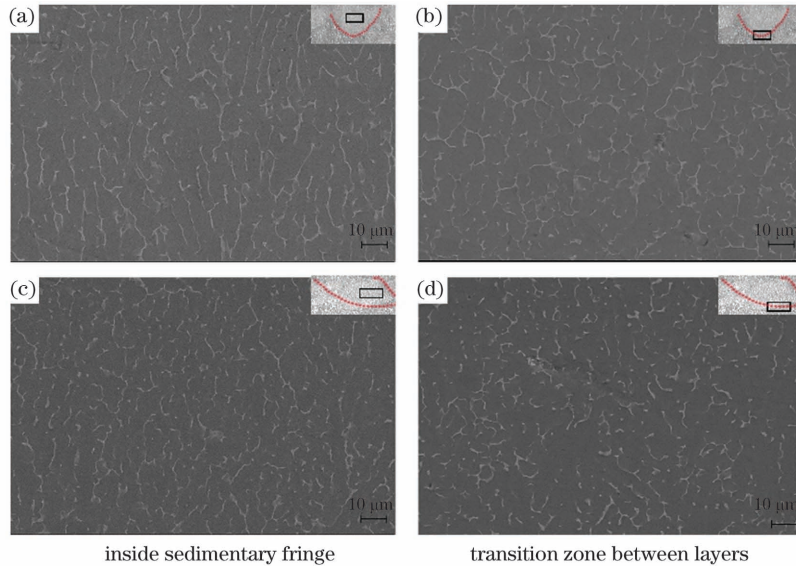


图 10 不同沉积路径下的 SEM 图。(a)(b)插补沉积;(c)(d)十字交叉沉积

Fig. 10 SEM images under different deposition paths. (a)(b) Unidirectional linear deposition; (c)(d) crisscross deposition

组织在低倍镜下的位置。图 10(a)是插补沉积下沉积条纹的内部组织,图 10(c)是十字交叉沉积下沉积条纹的内部组织,可以看出,两种不同沉积路径下的共晶组织均呈链状分布。图 10(b)是插补沉积下的层间过渡区域,可以看出,其共晶组织呈现链状分布,而十字交叉沉积下层间过渡区域[图 10(d)]的共晶组织呈现链状和骨骼状两种形态。从晶粒大小来看,插补沉积下的晶粒较小,而十字交叉沉积下有较多白色析出相。

前期凝固层受热发生重熔,Cu 元素不断析出,由于 α -Al 基体中共晶组织溶 Cu 能力有限,Cu 元素继续

以共晶组织存在^[14]。分析认为由于两种不同路径下沉积过程的受热方向不同,因此共晶组织的生长形态不同。采用插补沉积方法的增材过程,晶体的生长方向不发生改变,所以晶界处的共晶组织不断粗化,以骨骼状形成链状共晶。对于十字交叉沉积的增材过程,由于焊道方向发生了 90° 变化,晶体生长方向发生改变,Cu 元素偏析需要更多能量,故共晶组织以骨骼状和链状存在。

3.3 不同路径增材下的显微硬度分布

图 11 是两种沉积路径下的截面硬度分布云图,左

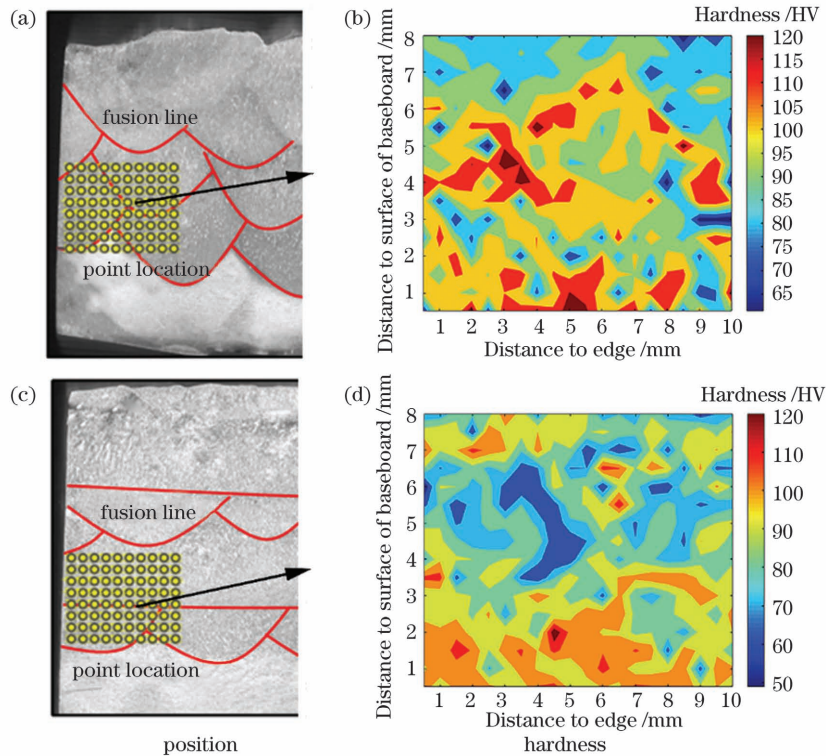


图 11 不同沉积路径下的硬度分布云图。(a)(b)插补沉积;(c)(d)十字交叉沉积

Fig. 11 Cloud maps of hardness distributions under different deposition paths. (a)(b) Unidirectional linear deposition; (c)(d) crisscross deposition

侧是测试硬度点的位置,可以看出,两种沉积路径下硬度分布从下到上总体呈现先高后低再高的趋势。图 11(a)是插补沉积下横截面的硬度分布图,其中硬度值最大值为 128.8 HV,最小值为 61.3 HV,平均值为 97.9 HV。图 11(b)是十字交叉沉积下横截面的硬度分布图,其中硬度值最大值为 128.0 HV,最小值为 60.2 HV,平均值为 89.2 HV。可以发现,插补沉积下每层的硬度分布不均匀,会在较小的区域产生硬度突变;十字交叉沉积下的硬度分布较插补沉积更均匀,硬度值整体偏低,且有较大面积的软化区域。

从光学显微镜中可以看出,插补沉积下的晶粒较十字交叉沉积下的晶粒更细小,而晶界处共晶相的厚度、长度及数量又会影响晶粒间的结合强度,进而影响焊缝力学性能^[19-20]。分析认为,由于插补沉积下成形合金试样的致密度高,因此整体硬度偏高。两种沉积路径下整体组织从下到上依次是细小等轴晶-柱状晶-粗大的等轴晶-细小的树枝晶,导致硬度变化趋势是先高后低再高。插补沉积下的硬度在水平方向上时高时低,这是由于沉积时熔合线为鱼鳞状,熔合线附近晶粒粗大,缺陷较多,硬度低,故低硬度区与熔合线重合。十字交叉沉积下熔合线有条状区,且熔合区较宽,故硬度分布中部出现较大的低硬度区。十字交叉沉积下出现大面积软化区,这是由于不同方向的沉积会产生较

多缺陷,故硬度较低。

3.4 不同沉积路径增材下的拉伸性能及断口形貌

图 12 为两种不同沉积路径下的拉伸性能图,其中插补沉积试件沿 X 轴方向的抗拉强度为 233.58 MPa,延伸率为 6.34%;沿 Y 轴方向的抗拉强度为 275.52 MPa,延伸率为 11.12%。十字交叉沉积试件在 XY 平面的极限抗拉强度为 251.33 MPa,延伸率为 7.68%。图 13 是两种沉积路径下沿 Y 轴方向的断口形貌,经过 EDS 分析可以发现,在韧窝中间析出的白色颗粒为 θ 强化相及 θ 相与共晶组织的混合相,韧窝边缘是 Al-Al₂Cu 共晶组织。

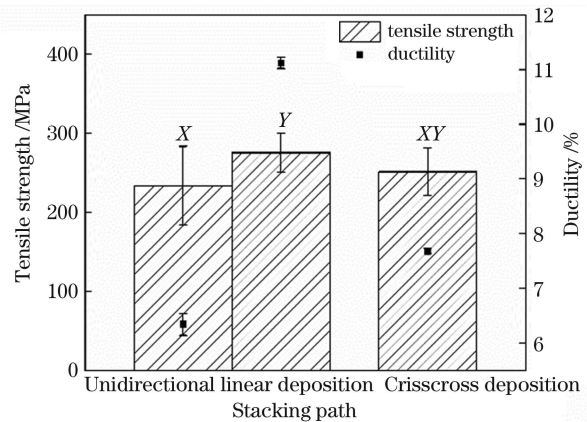


图 12 拉伸性能

Fig. 12 Tensile property

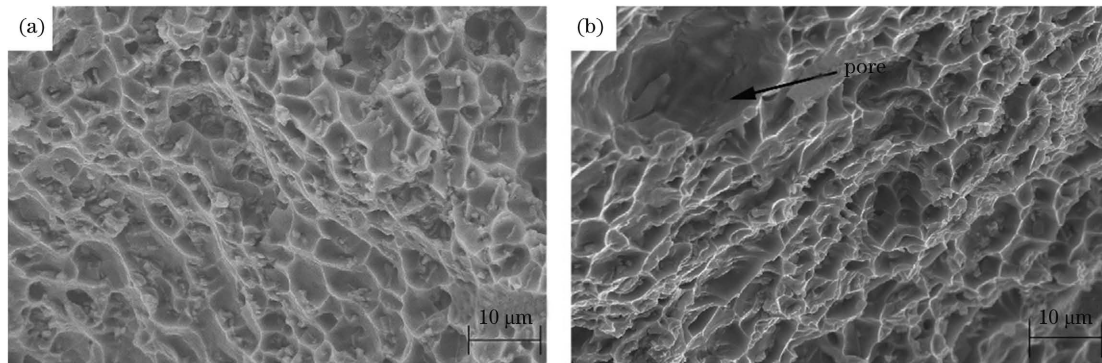


图 13 不同沉积路径下拉伸试件的断口 SEM 图。(a)插补沉积;(b)十字交叉沉积

Fig. 13 SEM images of fractures for tensile test specimens under different deposition paths. (a) Unidirectional linear deposition; (b) crisscross deposition

在沉积过程中,插补沉积下焊接方向均沿 Y 轴方向,而十字交叉沉积下相邻层的焊接方向分别沿 X 轴和 Y 轴方向,故插补沉积下的拉伸性能具有各向异性,十字交叉沉积下的拉伸性能具有各向同性。插补沉积下 X 轴方向的熔池边界混乱,重熔区较多,层间易形成气孔缺陷,故性能较差;插补沉积下 Y 轴方向的沉积层过渡较少,性能较好。晶界处分布的共晶组织沿着晶界生长,形态呈颗粒状-骨骼状-网状,随着固溶体形态的变化而出现缺陷^[21]。十字交叉沉积下晶界处有两种形态共晶组织,更易形成缺陷。从微观组织上可以看出,插补沉积下的晶粒更细小致密,而十字交叉沉积下的晶粒更粗大。由于变形过程中产生的大

应变力会促进微裂纹扩散^[22],十字交叉沉积下断口处出现较大孔洞,更易断裂,同时插补沉积下的韧窝更均匀致密,故十字交叉沉积下 Y 轴方向的性能较插补沉积下的差。

4 结 论

激光诱导 MIG 电弧复合技术使用两种不同的沉积路径。在宏观形貌上,插补沉积路径下的横截面表现出均匀的鱼鳞状,沉积条纹的分布较为均匀,熔宽和熔深相差不大;十字交叉沉积下的横截面呈鱼鳞状和条状交替出现,不同方向的沉积层熔深有明显差别。在微观组织上,两种沉积路径下的整体组织从下到上

依次是细小等轴晶-柱状晶-粗大的等轴晶-细小的树枝晶;插补沉积下的晶粒更细小,柱状晶生长方向一致,表现为各向异性;十字交叉沉积下的晶粒较粗大,柱状晶的生长方向杂乱无章,表现为各向同性。两种沉积路径下截面的维氏硬度从下到上整体呈先高后低再高的变化趋势。插补沉积下的平均硬度高于十字交叉沉积,而十字交叉沉积下的硬度分布更为均匀。根据拉伸测试结果,可以发现,插补沉积试件的强度和塑性具有各向异性,十字交叉沉积试件的强度和塑性具有各向同性。从扫描电镜结果分析得出,插补沉积下的断口韧窝更均匀,而十字交叉沉积下断口处出现了较大的孔洞,易形成微裂纹,故拉伸性能较差。

参 考 文 献

- [1] Buchanan C, Gardner L. Metal 3D printing in construction: a review of methods, research, applications, opportunities and challenges[J]. *Engineering Structures*, 2019, 180: 332-348.
- [2] 马驰, 刘永红, 纪仁杰, 等. 电弧增材制造综述: 技术流派与展望[J]. *电加工与模具*, 2020(4): 1-11.
Ma C, Liu Y H, Ji R J, et al. Review of wire and arc additive manufacturing: technology genre and prospect [J]. *Electromachining & Mould*, 2020(4): 1-11.
- [3] 秦艳利, 孙博慧, 张昊, 等. 选区激光熔化铝合金及其复合材料在航空航天领域的研究进展[J]. *中国激光*, 2021, 48(14): 1402002.
Qin Y L, Sun B H, Zhang H, et al. Development of selective laser melted aluminum alloys and aluminum matrix composites in aerospace field[J]. *Chinese Journal of Lasers*, 2021, 48(14): 1402002.
- [4] 侯世忠, 李雪峰. 铝合金丝材电弧增材制造技术的研究与应用[J]. *铝加工*, 2020(5): 3-8.
Hou S Z, Li X F. Research and application of aluminum alloy wire arc additive manufacturing [J]. *Aluminium Fabrication*, 2020(5): 3-8.
- [5] Cong B Q, Ding J L, Williams S. Effect of arc mode in cold metal transfer process on porosity of additively manufactured Al-6.3%Cu alloy [J]. *The International Journal of Advanced Manufacturing Technology*, 2015, 76(9/10/11/12): 1593-1606.
- [6] Hönnige J R, Colegrove P A, Ganguly S, et al. Control of residual stress and distortion in aluminium wire + arc additive manufacture with rolling [J]. *Additive Manufacturing*, 2018, 22: 775-783.
- [7] Fixter J, Gu J, Ding J, et al. Preliminary investigation into the suitability of 2xxx alloys for wire-arc additive manufacturing [J]. *Materials Science Forum*, 2016, 877: 611-616.
- [8] Ren L L, Gu H M, Wang W, et al. Effects of interpass cooling on material properties of wire arc additive manufactured Al-6.3Mg alloy [J]. *3D Printing and Additive Manufacturing*, 2019, 6(6): 344-353.
- [9] Wu B T, Pan Z X, Ding D H, et al. Effects of heat accumulation on microstructure and mechanical properties of Ti6Al4V alloy deposited by wire arc additive manufacturing [J]. *Additive Manufacturing*, 2018, 23: 151-160.
- [10] 李旭文, 宋刚, 张兆栋, 等. 激光诱导电弧复合增材制造 316 不锈钢的组织性能 [J]. *中国激光*, 2019, 46(12): 1202006.
Li X W, Song G, Zhang Z D, et al. Microstructure and properties of 316 stainless steel produced by laser-induced arc hybrid additive manufacturing [J]. *Chinese Journal of Lasers*, 2019, 46(12): 1202006.
- [11] Li R S, Zhang H O, Dai F S, et al. End lateral extension path strategy for intersection in wire and arc additive manufactured 2319 aluminum alloy [J]. *Rapid Prototyping Journal*, 2019, 26(2): 360-369.
- [12] 刘黎明, 贺雅净, 李宗玉, 等. 不同路径下 316 不锈钢电弧增材组织和性能 [J]. *焊接学报*, 2020, 41(12): 13-19, 97.
Liu L M, He Y J, Li Z Y, et al. Research on microstructure and mechanical properties of 316 stainless steel fabricated by arc additive manufacturing in different paths [J]. *Transactions of the China Welding Institution*, 2020, 41(12): 13-19, 97.
- [13] Thijs L, Kempen K, Kruth J P, et al. Fine-structured aluminium products with controllable texture by selective laser melting of pre-alloyed AlSi10Mg powder [J]. *Acta Materialia*, 2013, 61(5): 1809-1819.
- [14] Prashanth K G, Scudino S, Eckert J. Defining the tensile properties of Al-12Si parts produced by selective laser melting [J]. *Acta Materialia*, 2017, 126: 25-35.
- [15] 孙承帅, 张兆栋, 刘黎明. 激光功率对 5356 铝合金激光诱导 MIG 电弧增材制造组织性能的影响 [J]. *焊接学报*, 2018, 39(9): 13-18, 129.
Sun C S, Zhang Z D, Liu L M. Effect of laser power on microstructure and properties of 5356 aluminum alloy by laser induced MIG arc additive manufacturing [J]. *Transactions of the China Welding Institution*, 2018, 39(9): 13-18, 129.
- [16] 柏久阳. 2219 铝合金 GTA 增材制造及其热处理过程的组织演变 [D]. 哈尔滨: 哈尔滨工业大学, 2017.
Bai J Y. Microstructure evolution of 2219-Al during GTA based additive manufacturing and heat treatment [D]. Harbin: Harbin Institute of Technology, 2017.
- [17] Wu D J, Liu D H, Niu F Y, et al. Al-Cu alloy fabricated by novel laser-tungsten inert gas hybrid additive manufacturing [J]. *Additive Manufacturing*, 2020, 32: 100954.
- [18] Zhang W Y. *Welding metallurgy* [M]. Beijing: Machinery Industry Press, 1999: 164-166.
- [19] Li Q, Wu A P, Li Y J, et al. Segregation in fusion weld of 2219 aluminum alloy and its influence on mechanical properties of weld [J]. *Transactions of Nonferrous Metals Society of China*, 2017, 27(2): 258-271.
- [20] Liu D H, Wu D J, Ma G Y, et al. Effect of post-deposition heat treatment on laser-TIG hybrid additive manufactured Al-Cu alloy [J]. *Virtual and Physical Prototyping*, 2020, 15(4): 445-459.
- [21] 张文明, 韩嘉伟. 2319 铝合金电弧增材制造成型和组织 [J]. *沈阳大学学报(自然科学版)*, 2020, 32(3): 194-199.
Zhang W M, Han J W. 2319 aluminum alloy arc additive manufacturing forming and microstructure [J]. *Journal of Shenyang University (Natural Science)*, 2020, 32(3): 194-199.
- [22] Gu J L, Yang S L, Gao M J, et al. Micropore evolution in additively manufactured aluminum alloys under heat treatment and inter-layer rolling [J]. *Materials & Design*, 2020, 186: 108288.

Effect of Stacking Path on Laser Induced MIG Additive 2319 Aluminum Alloy

Jin Peixin, Zhang Zhaodong^{*}, Ma Zicheng, Song Gang, Liu Liming

Key Laboratory of Advanced Connection Technology of Liaoning Province, School of Materials Science and Engineering, Dalian University of Technology, Dalian 116024, Liaoning, China

Abstract

Objective Arc additive manufacturing has the advantages such as high stacking rate, high material utilization rate, low equipment cost, and ability to manufacture large components. Aluminum alloy parts with complex structures can be made by wire arc additive manufacturing (WAAM). What is more, WAAM can directly produce a complete component, which greatly simplifies the processing process. However, the aluminum alloy component made by WAAM has the defects of poor forming quality, many defects, and low mechanical properties, while the laser induced arc composite additive (LIACD) technology can effectively improve the forming quality and mechanical properties. Recently, most of research on WAAM of aluminum alloys is still focused on single-channel multi-layer thin-walled parts, but there are few researches on multi-channel and multi-layer arc additive manufacturing. Path strategy is the first step of WAAM. In the case of multi-layer and multi-channel, the heat dissipation conditions of different stacking paths are different, resulting in changes in the microstructures and properties of specimens and thus influencing the application fields. The LIACD manufacturing technology is based on arc and supplemented by a laser, which can further improve the forming quality and mechanical properties of arc additive manufacturing. In this paper, the laser induced MIG composite additive manufacturing technology is used to fabricate 2319 aluminum alloys. The effects of two deposition paths, namely unidirectional linear deposition and crisscross deposition, on the microstructures and properties of 2319 aluminum alloy blocks are studied.

Methods In this study, a low power pulsed laser-MIG composite heat source is used for resurfacing welding of ER2319 welding wires on the 2219 aluminum alloy substrate. The protective gas used in this experiment is Ar with a mass fraction of 99.99% and a flow rate of 20 L/min. The welding current is 140 A, the average laser power is 300 W, the scanning speed is 450 mm/min, the wire feeding speed automatically matches the welding current, the inter-channel overlap rate is 25%, and the wire dry elongation is 11 mm. The interlayer cooling time is 60 s after each layer is stacked, and the inter-channel cooling time is 30 s after each layer is stacked. Two paths of unidirectional linear deposition and crisscross deposition are selected to make the aluminum alloy blocks. The two groups of samples are wire cut. The crisscross sections of these samples are first grinded with sandpaper and then polished and etched successively. The microstructures and fracture morphologies are observed under optical microscope and scanning electron microscope, respectively. The mechanical properties of these two groups of specimens are tested by the micro-hardness tester and the universal tensile test machine. The microstructures and fractography of the two groups of samples are analyzed by energy disperse spectroscopy (EDS).

Results and Discussions As for the macroscopic forming quality, as shown in Fig. 5(a), for the unidirectional linear deposition, there exists a uniform fish scale shape in its cross section and obvious wave lines between layers. As shown in Fig. 5(b), for the crisscross deposition, there exist fish scales and strips alternating in cross section. In terms of microstructures (Figs. 6, 7, 8 and 10), the grains for the unidirectional linear deposition are smaller, and the growth direction of the columnar crystals is consistent. The pores are mainly distributed in the transition region between deposition layers, and the eutectic structures at the grain boundary present a chain distribution. The grains for the crisscross deposition are relatively thick and the distribution of columnar crystals is disorderly. The eutectic structures at the grain boundary show two forms of chain and bone, and the distribution of stomatal defects is wide. Because of the addition of a pulsed laser, a layer of fine equiaxed crystal region is generated between layers, and the distribution of the equiaxed crystal region for the unidirectional linear deposition is continuous, while the cross distribution is discontinuous. The difference in mechanical property for two paths can be seen from the cloud maps of hardness distribution (Fig. 11). The overall hardness distribution for two paths shows a trend of first high, then low, and finally high from bottom to top, and the porosity has a great influence on hardness. This phenomenon is related to the change of grain morphology at different positions of the sample. There is a large softening zone in the crisscross, indicating that the porosity defect has a great influence on the hardness distribution.

Conclusions Observed from the macroscopic morphology, the grain size of the microstructures for the unidirectional linear deposition is smaller and the defects are less than those for the crisscross deposition. In terms of performance, the average hardness for the unidirectional linear deposition is 97.9 HV, and that for the crisscross deposition is 89.2 HV.

The strength and plasticity for the unidirectional linear deposition specimens are anisotropic, while those for the crisscross deposition specimens are isotropic. The tensile strength for the unidirectional linear deposition specimens sampled along the X -axis is 233.58 MPa, and the elongation is 6.34%. The tensile strength sampled along the Y -axis is 275.52 MPa, and the elongation is 11.12%. The ultimate tensile strength for the crisscross deposited specimens sampled in the XY plane is 251.33 MPa, and the elongation is 7.68%. From the tensile property diagram (Fig. 12) and the SEM fractography for the tensile test specimens (Fig. 13), it is found that the crisscross plasticity is poor, and the large holes appear at the fracture, which influences the performance. The results show that the overall microstructure and properties of the aluminum alloy blocks in the Y -axis direction produced by laser induced MIG additive manufacturing unidirectional linear deposition are higher than those obtained by crisscross deposition.

Key words laser technique; laser induced arc; path; additive manufacturing; 2319 aluminum alloy; microstructure and property; scanning electron microscope